Parameter Sensitivity in Control Allocation: A Monte Carlo Analysis for an Over-Actuated Aerial Robot

S. Al-zubaidi*, J. Skinner, and K. A. Stol
Faculty of Engineering, University of Auckland

ABSTRACT

Physical parameter uncertainty can degrade control allocation in over-actuated aerial vehicles by producing tracking error and cross-axis coupling. We present a Monte Carlo sensitivity study for a fixed-tilt octocopter, linking realistic motor/ESC, mass, inertia, centre-of-mass, and environmental variations to steady-state wrench error. For the tested platform and fixed allocator, vertical CoM displacement and inter-motor asymmetry dominate allocation degradation. The results provide practical guidance for mechanical tolerance control, actuator matching, and targeted calibration, while clarifying which conclusions are specific to this UAV and which may transfer to related over-actuated multirotor designs.

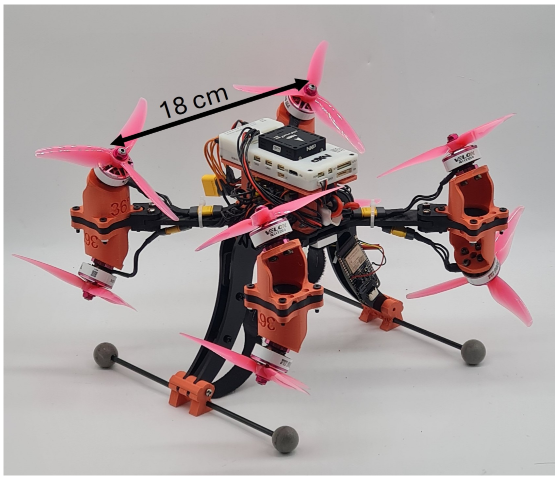

Figure 1: The stacked octocopter platform used in this study.

1 INTRODUCTION

Unmanned Aerial Vehicles (UAVs) have advanced significantly as demand for industrial applications grows [1]. As the scope of work for UAVs expands into precision agriculture, infrastructure inspection, and autonomous manipulation, demands for accuracy, safety, and performance have increased proportionally. The evolution of UAV airframe design has produced over-actuated configurations that enable control over all six degrees of freedom (DoF), allowing independent manipulation of position and orientation [2, 3].

Over-actuated UAVs, such as the example shown in Fig. 1, offer significant advantages over conventional quadrotors. The decoupling of position and orientation control enables precise end-effector positioning while maintaining arbitrary orientation, essential for applications such as aerial manipulation, inspection with directional sensors, or grasping tasks. Fully-actuated systems also provide higher bandwidth in horizontal axes that typically rely on attitude response in underactuated platforms, improving stability in dynamic environments such as turbulent wind [4]. Additionally, actuator redundancy provides fault tolerance and enables optimisation of secondary objectives such as power consumption or actuator wear.

However, over-actuated systems, in which the number of actuators exceeds the degrees of freedom, present challenges for control allocation. Because multiple actuator combinations can produce the same motion, the task of distributing control commands (known as *control allocation*) becomes more complex. Control allocation maps desired forces and moments from a high-level controller to actuator commands while respecting constraints such as saturation and rate limits [5]. For over-actuated systems where the effectiveness matrix $\mathbf{B}$ has more columns than rows, infinitely many solutions exist. Traditional methods, such as direct matrix inversion via the Moore-Penrose pseudoinverse, often perform poorly in these scenarios, yielding suboptimal solutions or, in critical cases, actuator saturation that degrades overall control performance [5].

Various approaches have been developed to address these challenges. Traditional methods include explicit ganging [6], daisy-chaining [7], and pseudoinverse-based mixing. The redistributed pseudoinverse iteratively clamps saturated actuators and recomputes the allocation, but early clipping errors can irreversibly degrade control performance [8]. Optimisation-based methods formulate control allocation as a constrained problem: direct allocation preserves commanded moment direction under saturation [9], while error minimisation directly prioritises tracking accuracy. Quadratic programming (QP) provides a convex, well-posed formulation that enforces actuator constraints robustly [10]. Adaptive methods address actuator uncertainty without explicit fault detection, with continuous adaptation modelling actuator ef-

*Email address: salim.al-zubaidi@auckland.ac.nz

fectiveness as uncertain and updating allocation parameters using tracking errors [11]. Fault-triggered schemes integrate with fault detection systems to reconfigure allocation upon actuator failure [12].

For over-actuated UAVs, accurate knowledge of physical parameters (mass distribution, centre of gravity, inertia, and actuator characteristics) strongly influences control allocation performance. If the internal model is inaccurate, cross-axis coupling, tracking errors, and instability can result, particularly when using model-based control techniques such as Model Predictive Control (MPC) or Incremental Nonlinear Dynamic Inversion (INDI) [13]. These challenges are especially relevant for fully actuated and tilted-rotor multirotors, where non-vertical thrust components make allocation errors visible across multiple force and torque axes.

While allocation algorithms are well-studied, systematic quantification of parameter sensitivities remains limited. Most validation studies focus on conventional or under-actuated platforms and assume known nominal parameters or focus on fault tolerance rather than the impact of realistic manufacturing tolerances and operational variations. Fixed-tilt multirotors and heterogeneous propulsion configurations introduce unique challenges including increased actuator coupling, nontrivial mapping between thrust inputs and resulting dynamics, and the potential for internal redundancy to obscure parameter observability [14]. Few works offer direct comparisons of allocation methods on common over-actuated platforms or quantify which specific physical parameters most critically affect allocation performance, making it difficult to assess practical trade-offs in real deployment scenarios.

This paper addresses these gaps with a systematic, airframe-specific sensitivity analysis for a fixed-tilt stacked octocopter (Fig. 1). The main contribution is a Monte Carlo sensitivity analysis that identifies which physical parameters dominate allocation error, enabling targeted calibration, tolerance specification, and design optimisation. Parameter distributions are derived from manufacturer data, operational experience, and literature. A step-by-step simulation workflow connects sampled motor, ESC, airframe, CoM, and environmental parameters to steady-state force and torque output, clarifying how parameter deviations produce allocation errors. The resulting design guidance includes explicit bounds on generality: the numerical ranking is platform- and allocator-dependent, while the workflow can be repeated for other UAVs and allocation laws.

2 Platform and Steady-State Model

2.1 *Stacked Octocopter Platform*

The platform is a custom-built over-actuated UAV with eight rotors arranged in two layers [14]. The upper rotors are tilted around the x-axis, while the lower rotors are tilted around the y-axis (Fig. 1). This fixed-tilt design provides full 6-DoF control authority without requiring variable-tilt mechanisms. The body frame follows the North-East-Down (NED) convention with the x-axis pointing forward, y-axis to the right, and z-axis downward.

Table 1: Nominal Physical Parameters

Parameter	Symbol	Value
Mass	m	0.95 kg
Inertia (Roll)	I_{xx}	0.024 kg·m^2
Inertia (Pitch)	I_{yy}	0.024 kg·m^2
Inertia (Yaw)	I_{zz}	0.105 kg·m^2
Arm Length	L	0.125 m
Rotor Tilt Angle	α	32°
Propeller Diameter	D_{prop}	5 × 4.5 inch

The hardware consists of BE-ox V32306 2250 kV motors with 5×4.5 inch propellers, 50A ESCs with bidirectional DShot. Table 1 summarises the key physical parameters.

2.2 *Steady-State Wrench Model*

In this study, control allocation is represented by a fixed nominal mixer matrix $\mathbf{\Gamma}$. The matrix is designed for the nominal geometry and is held constant during all uncertainty trials; therefore, the results quantify robustness of this control allocation method. The desired control setpoint $\tilde{\mathbf{u}}$ is mapped to individual motor commands as:

$$\mathbf{c}_{\text{norm}} = \text{clip}\left(\mathbf{\Gamma}\tilde{\mathbf{u}}, -1, 1\right) \tag{1}$$

The normalised command is scaled to the PWM input $\mathbf{u}_{\text{dyn}} = (\mathbf{c}_{\text{norm}} + 1)/2$. For each Monte Carlo trial, $\mathbf{\Gamma}$ remains unchanged while the physical plant parameters are perturbed. This captures a practical deployment scenario: an allocator is designed from nominal CAD and component data, but the real vehicle differs from that model.

The motor dynamic equation relates angular acceleration to electrical and mechanical torques:

$$J\dot{\omega} = \frac{K_t}{R}(uV_{\text{batt}} - K_e\omega) - K_t I_0 - C_\tau \omega^2 \tag{2}$$

where J is rotor inertia, K_t and K_e are torque and back-EMF constants, R is winding resistance, I_0 is no-load current, and C_τ is the propeller torque coefficient. At steady state ($\dot{\omega} = 0$), this quadratic balance is solved for the physically meaningful positive root $\omega_{ss,i}(u_i)$ for each motor. Thus K_t, K_e, R, I_0, C_τ, and ESC voltage mapping parameters influence the final wrench by first changing each motor's steady-state speed, then changing thrust and reaction torque through the squared-speed terms below.

Each motor produces thrust and reaction torque in its local frame:

$$^{m_i}\mathbf{T}_i = \begin{bmatrix} 0 \\ 0 \\ -k_f\omega_{ss,i}^2 \end{bmatrix}, \quad ^{m_i}\boldsymbol{\tau}_i = \begin{bmatrix} 0 \\ 0 \\ -d_{r,i}C_\tau\omega_{ss,i}^2 \end{bmatrix} \tag{3}$$

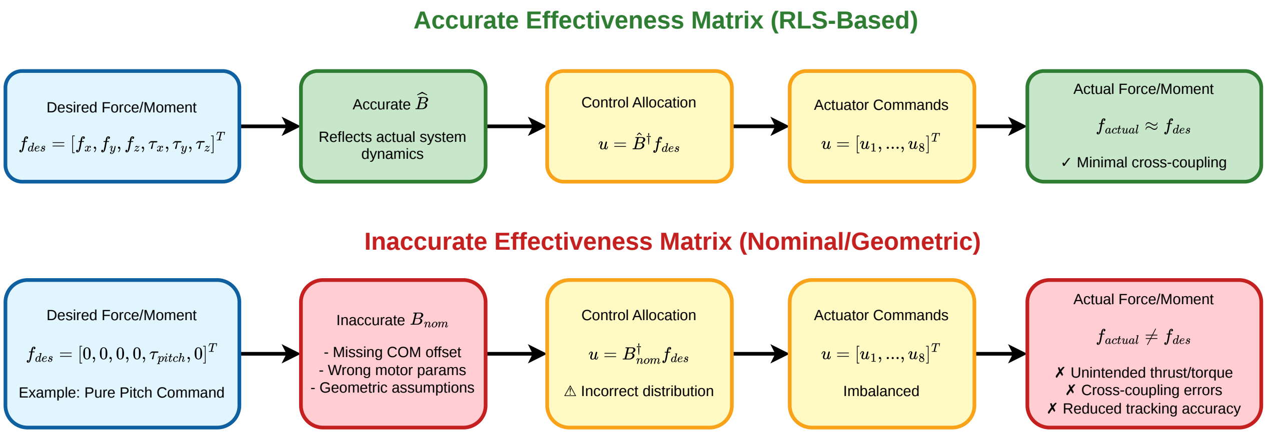

Figure 2: Control allocation error propagation: inaccuracies in the effectiveness matrix lead to incorrect actuator distribution, cross-axis coupling, and degraded tracking performance.

where $d_{r,i} \in \{-1, +1\}$ indicates rotation direction and $k_f = 0.5\rho p_{z3} D^2_{prop} A_p$.

The total body-frame wrench sums contributions from all motors, transformed from motor frames:

$$^{b}\mathbf{T}_{ss} = \sum_{i=1}^{8} \mathbf{R}_{m_i \to b} \cdot {}^{m_i}\mathbf{T}_i \tag{4}$$

$$^{b}\boldsymbol{\tau}_{ss} = \sum_{i=1}^{8} \left(\mathbf{R}_{m_i \to b} \cdot {}^{m_i}\boldsymbol{\tau}_i + \mathbf{r}_i \times (\mathbf{R}_{m_i \to b} \cdot {}^{m_i}\mathbf{T}_i)\right) \tag{5}$$

where $\mathbf{r}_i$ is the position vector from the Centre of Mass (CoM) to motor i. CoM perturbations enter through this moment arm, motor-axis geometry enters through $\mathbf{R}_{m_i \to b}$, and environmental and propeller parameters enter through k_f. Consequently, the same command vector can produce a different body wrench even though the allocator command is unchanged.

2.3 *Simulation Workflow*

Each simulation trial proceeds as follows:

1. Sample one vehicle instance from Table 2. Motor parameters are sampled independently; while the rest of the parameters are sampled at vehicle level.
2. Apply the fixed nominal mixer $\boldsymbol{\Gamma}$ to one representative setpoint to obtain clipped motor commands.
3. Convert each normalised command to a PWM input and solve Eq. 2 to find steady-state motor speed.
4. Convert each speed to local thrust and reaction torque, then transform these contributions into the body frame using Eqs. 4–5.
5. Normalise the resulting physical wrench and compute error and leakage scores.

3 Sensitivity Analysis Methodology

3.1 *Sources of Parameter Uncertainty*

Physical parameters are subject to variation from four primary sources:

- **Manufacturing tolerances**: Motor constants (K_V, K_E, C_τ) vary between units even within the same batch [15].
- **Assembly inconsistencies**: CoM shifts due to battery placement, cable routing, and component mounting.
- **Degradation**: Demagnetization reduces motor constants; bearing wear increases no-load current [16].
- **Environmental factors**: Air density varies with temperature, pressure, and altitude.

3.2 *Monte Carlo Simulation*

For each of $N = 10{,}000$ trials, every parameter was sampled from a normal distribution centred on its nominal value. The standard deviations in Table 2 are derived from manufacturer specifications, operational experience, and literature.

The 10% variation for I_0 (no-load current) is based on Portescap datasheet values and is assumed representative across brands.

Motor-specific parameters were sampled *independently for each motor* to capture inter-motor discrepancies. This enables analysis of both symmetric shifts (all motors deviate together) and asymmetric spread (motors differ from each other).

3.3 *Justification of Selected Variations*

The standard deviations in Table 2 model realistic operational uncertainty based on manufacturer data, literature, and operational experience.

Table 2: Parameter Variations for Monte Carlo Simulation

Parameter	**Variation (σ)**	**Source**
Motor & ESC (per-motor)		
K_V, K_E, C_τ	3.0%	[16]
R (Resistance)	5.0%	[15]
I_0 (No-load current)	10.0%	Portescap datasheet
V_{off}, m_v (ESC)	2.0%	[17]
D_{prop}	1.0%	[18]
Airframe & Mass		
Mass (M)	2.0%	[19]
Inertia (I)	5.0%	[20]
CoM X, Y	1 mm (abs)	[21]
CoM Z	10 mm (abs)	Operational
Environmental		
ρ_{air}	10.0%	Atmospheric

Motor & ESC Parameters: Motor electromagnetic constants (K_V, K_E, C_τ) use 3% variation reflecting manufacturing tolerance and degradation (demagnetization) [16]. Resistance (R) uses 5% due to thermal effects and winding health variations [22]. No-load current (I_0) uses 10% due to bearing friction sensitivity. ESC voltage mapping (V_{off}, m_v) uses 2% from component tolerances [17]. Motor-specific parameters were sampled independently per motor to capture both symmetric shifts (all motors deviate together) and asymmetric spread (motors differ from each other). For each parameter in each trial, features were computed as: (1) *MeanDev*—mean absolute deviation from nominal across all motors, quantifying overall magnitude of shift; (2) *StdDev*—standard deviation of sampled values across motors, quantifying inter-motor variability; (3) *Range*—difference between maximum and minimum sampled values across motors, quantifying spread extremes. Symmetric shifts affect peak performance; asymmetric spread drives cross-axis leakage.

Airframe & Mass: Mass uses 2% for added hardware/cables beyond CAD. Inertia uses 5% from measurement and CAD estimation uncertainty. CoM uses absolute deviations $[1, 1, 10]$ mm (X,Y,Z), with larger vertical tolerance reflecting battery mounting variability (brand/size differences, velcro strap positioning).

Environmental: Air density uses 10%, combining barometric pressure fluctuations ($\pm$20–30 hPa $\rightarrow \pm 3\%$) and temperature swings (20°C $\rightarrow \pm 5\%$) [23].

3.4 Performance Metrics

Two metrics quantify allocation degradation. Since the desired setpoint $\mathbf{W}_{\text{desired}}$ is a unitless vector (normalised to [-1, 1] except for F_z which is [0, 1]), while the system output $\mathbf{W}_{\text{actual}}$ consists of physical forces (N) and torques (Nm), the output must first be normalised to enable meaningful comparison.

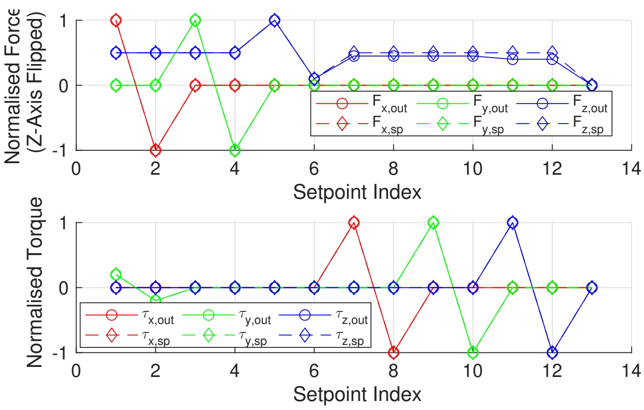

Figure 3: Normalisation of output wrench components. Physical forces (F_x, F_y, F_z in N) and torques (τ_x, τ_y, τ_z in Nm) are scaled to unitless ranges matching commanded setpoints: [-1, 1] for x/y forces and torques, [0, 1] for z-force.

For the five axes with zero-centred command ranges ($F_x, F_y, \tau_x, \tau_y, \tau_z$), normalisation is performed by scaling against the vehicle's maximum authority:

$$[\mathbf{W}_{\text{actual, norm}}]_i = \frac{[\mathbf{W}_{\text{actual}}]_i}{[\mathbf{W}_{\text{max}}]_i} \quad \text{for } i \in \{1, 2, 4, 5, 6\} \tag{6}$$

For the vertical thrust axis (F_z), a min-max scaling accounts for a non-zero thrust offset identified during nominal characterisation:

$$[\mathbf{W}_{\text{actual, norm}}]_3 = \frac{[\mathbf{W}_{\text{actual}}]_3 - F_{z,\text{offset}}}{F_{z,\text{max}} - F_{z,\text{offset}}} \tag{7}$$

Figure 3 illustrates this normalisation, showing how physical force and torque outputs are mapped to the same unitless range as the commanded setpoints.

Normalised Error Score: The L2-norm of the difference between desired and normalised actual output:

$$S_{\text{Error}} = \|\mathbf{W}_{\text{actual, norm}} - \mathbf{W}_{\text{desired}}\|_2 \tag{8}$$

Relative Leakage Score: The magnitude of wrench components on axes commanded to zero, relative to the commanded wrench:

$$S_{\text{Leakage}} = \frac{\|\mathbf{W}_{\text{leakage}}\|_2}{\|\mathbf{W}_{\text{desired}}\|_2} \times 100\% \tag{9}$$

3.5 Test Setpoints

Six representative setpoints isolate each degree of freedom. All setpoints except pure vertical thrust include a 0.5 vertical thrust bias to operate around a typical hover point, linearising system behaviour around a common operating condition. Figure 3 shows the input setpoints.

3.6 Stepwise Multivariable Regression

To isolate each parameter's effect while accounting for confounding variables, stepwise multivariable linear regression with backward elimination was applied per setpoint [24].

For each setpoint, a full linear model predicts performance score (Y) from all parameter features ($X_1, \ldots, X_p$):

$$Y = \beta_0 + \beta_1 X_1 + \beta_2 X_2 + \cdots + \beta_p X_p + \epsilon \tag{10}$$

Predictors with $p > 0.05$ were iteratively removed via backward elimination until all remaining coefficients were significant. Backward elimination is preferred over forward selection as it captures interactions that might appear insignificant in isolation. While LASSO regression offers advantages in some contexts, it can arbitrarily select among correlated predictors, which would complicate interpretation when motor parameters within the same unit are physically correlated.

Models achieved adjusted R^2 values ranging from 0.21 to 0.38 (mean 0.31). These modest values are an important limitation and indicate that a linear additive model does not capture the full nonlinear structure of the simulator. In particular, the features used here (MeanDev, StdDev, and Range) summarise the magnitude of motor mismatch but not which physical motor locations contain the high or low values; two samples with the same spread can produce different leakage depending on their spatial arrangement. We therefore interpret regression outputs as sensitivity indicators rather than predictive performance models. Future code releases will make it straightforward to replace this stage with higher-capacity models such as Gaussian processes, random forests, or polynomial chaos expansions, while retaining the same simulation workflow.

Final models were aggregated by *frequency* (percentage of setpoint models where a parameter remained significant) and *strength* (mean absolute t-statistic when significant), distinguishing localised vs. distributed effects.

4 RESULTS

4.1 Nominal System Characterisation

The nominal system (all parameters at their specified values) was first characterised to establish baseline performance. A key finding was a non-zero thrust offset at zero command input, confirming linear response but requiring specialised normalisation for the F_z axis (Fig. 4).

4.2 Overall Parameter Sensitivity

Figure 5 aggregates results from all per-setpoint regression models, showing both the *frequency* at which each parameter was statistically significant and the *average strength* (mean absolute t-statistic) of its effect.

The results reveal a clear hierarchy of parameter sensitivities. Uncertainty in the vehicle's Centre of Mass (CoM) was found to be the dominant driver of both overall wrench error and cross-axis leakage. Secondary, yet still significant factors included inter-motor discrepancies, specifically the standard deviation of the back-EMF constant (`StdDev_KE`). Other motor parameters show smaller but consistent influences, with effects occurring uniformly across most manoeuvre setpoints rather than being manoeuvre-specific. In contrast, the system demonstrated robustness to environmental variations such as air density.

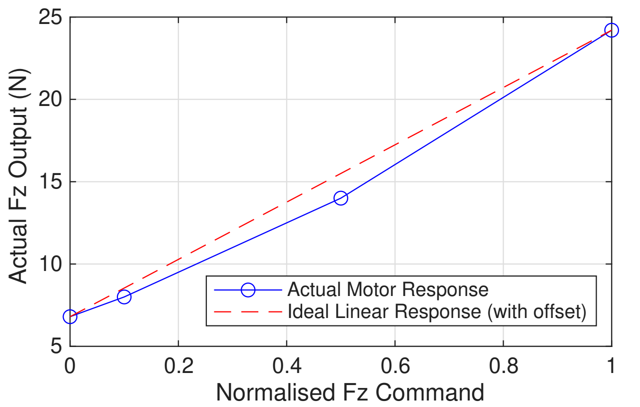

Figure 4: Physical thrust output vs. normalised F_z command for the nominal model.

4.3 Key Findings

1. Vertical CoM Displacement Dominates: Centre of Mass variation along the Z-axis (`CoM_AbsDev_Z`) is the strongest performance driver for this platform. This parameter particularly affects horizontal thrust manoeuvres (F_x, F_y). When CoM shifts vertically, tilted thrust vectors no longer pass through the centre of mass, creating coupling between translation and rotation. For this platform's 32° tilt angle, a 10 mm CoM shift generates parasitic moments the allocator cannot fully compensate. This sensitivity is geometry-dependent and manoeuvre-specific.

Figure 6 illustrates this effect for the F_y setpoint (horizontal thrust), showing a strong linear relationship ($R = 0.89$) between vertical CoM deviation and roll torque leakage. The physical mechanism: vertical CoM displacement changes the moment arm for motors producing horizontal thrust, directly generating parasitic roll moments proportional to the displacement.

2. Motor Asymmetry Causes Consistent Leakage: Inter-motor variations, especially in back-EMF (`StdDev_KE`), represent the second most significant factor. Unlike CoM, motor asymmetry affects setpoints universally. When motors have different electromagnetic constants, identical commands produce unequal thrusts, creating unintended force/torque components. This affects fundamental actuator response rather than geometric coupling.

3. Distributed Motor Effects: Other motor parameters show smaller but consistent influences across both leakage and error metrics, with effects occurring uniformly across most manoeuvre setpoints rather than being manoeuvre-

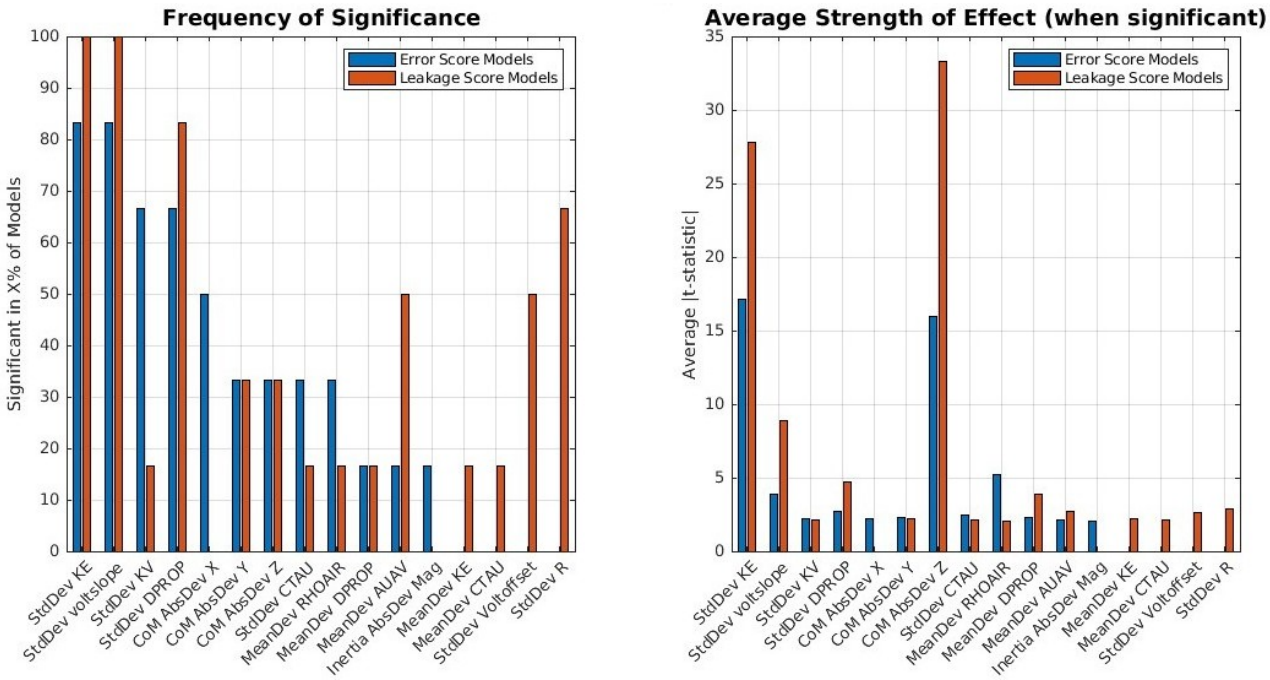

Figure 5: Overall parameter significance summary. **(Left)** Percentage of manoeuvre models in which each parameter remained significant after backward elimination. **(Right)** Average absolute t-statistic indicating typical effect strength.

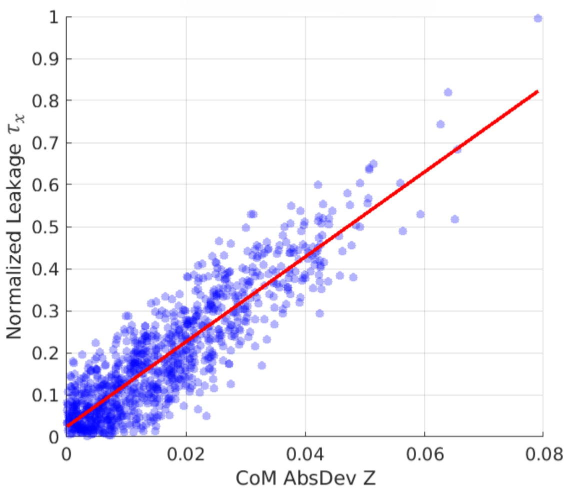

Figure 6: Vertical CoM deviation vs. normalised roll torque leakage for F_y setpoint (horizontal thrust).

specific.

4. Environmental Robustness: Air density was not statistically significant in any model. Symmetric changes (affecting all motors equally) preserve allocation geometry, so relative cross-coupling is unaffected unless approaching saturation.

5. Manoeuvre-Dependent vs. Universal Sensitivities: CoM affects specific manoeuvres (horizontal thrust), while motor asymmetry universally degrades performance. This distinction enables targeted mitigation: manoeuvre-dependent effects may be adaptively compensated, while universal effects require component matching or calibration.

5 DISCUSSION

5.1 *Implications for Practitioners*

The results suggest the following prioritisation for improving control allocation accuracy in over-actuated systems:

Mechanical Precision - Highest Priority: First, standardising mass distribution to minimise CoM variation. Secondly, the use of mechanical fixtures (jigs, bays, locking mechanisms) rather than flexible mounting (straps, velcro) to ensure the parts do not move around during flight keeping CoM fixed during flight.

Component Matching: First, characterise individual actuator parameters and match units with similar characteristics. For electric motors, the back-EMF constant (K_E) is most critical, as asymmetry in this parameter drives consistent cross-axis leakage across all manoeuvres. In addition, distributing matched actuators balances asymmetric effects and reduces leakage errors.

5.2 *Generalisability and Allocator Dependence*

The specific sensitivity rankings depend on both this platform's geometry (32° tilt, stacked configuration) and a fixed matrix as the control allocation. However, the methodology detailed in Section 3 can be repeated for other over-actuated UAVs and allocation methods. That said, several physical mechanisms are nevertheless expected to transfer across related aerial platforms:

1. CoM sensitivity: UAVs exhibit coupling between translational and rotational commands. This is particularly relevant for tilted-rotor and fully actuated multirotors. The dominant sensitivity axis varies with airframe geometry, but the underlying moment-arm mechanism is shared.

2. Actuator matching: Multi-rotor UAVs benefit from matched propulsion units, although the most critical motor or propeller parameter may vary with the airframe, motor model, and operating point.

3. Assembly vs. environment: Mechanical assembly precision is likely to dominate in controlled indoor UAV operation, while outdoor flight with large temperature, pressure, or wind variations may increase the relative importance of environmental uncertainty.

The Monte Carlo workflow presented here provides a template for quantifying sensitivities on other UAV platforms. The regression stage gives a compact, statistically interpretable summary, despite strong correlations. For this platform, the strongest mechanism was also visible directly in the simulator output, as evidenced by the strong correlation between vertical CoM deviation and observed roll leakage.

5.3 Experimental Check and Limitations

This analysis focuses on steady-state allocation performance and does not capture transient effects from motor dynamics (time constants, delays), aerodynamic rotor-rotor interactions or rate-constrained allocation behaviour near saturation. The regression analysis assumes linear superposition of parameter effects; nonlinear interactions may exist at extreme parameter deviations. The allocator is also fixed throughout the study, so conclusions about relative sensitivity should be re-evaluated for allocation methods with different constraint handling, null-space objectives, or adaptation.

A limited qualitative experimental check was conducted on a similar physical octocopter using motion-capture measurements during horizontal thrust manoeuvres with intentionally shifted battery/CoM placement. The observed cross-coupling direction was consistent with the simulation prediction that vertical CoM displacement induces parasitic roll/pitch moments during lateral force commands. This is not presented as quantitative validation because closed-loop controller compensation, motion-capture differentiation noise, and imperfect knowledge of the exact CoM shift prevented a clean comparison.

6 CONCLUSION

This paper presented a systematic uncertainty-to-wrench sensitivity workflow for quantifying how realistic parameter variations affect a fixed control allocator on an over-actuated fixed-tilt octocopter. Using Monte Carlo simulation with 10,000 samples and interpretable regression screening, we identified vertical Centre of Mass displacement and inter-motor asymmetries as the dominant factors degrading allocation accuracy and inducing cross-axis leakage for this platform and allocator.

For the tested platform, physical assembly precision and component matching had stronger effects on control allocation performance than aggregate mass properties or ambient conditions. Tightening vertical CoM tolerance (e.g., through standardised battery mounting) and matching motor electromagnetic constants offer practical routes to improved allocation accuracy.

These findings translate into design guidance for over-actuated UAVs: prioritise mechanical consistency in mass distribution, characterise and match actuators before assembly, and focus calibration on inter-unit variations rather than environmental compensation. While the specific sensitivity rankings depend on airframe geometry and allocation law, the workflow can be applied to related multirotor UAV designs.

Future work will extend this analysis in four directions. First, incorporating motor dynamics and transient responses will capture time-dependent effects during rapid manoeuvres. Second, load-cell or thrust-stand validation will quantify the predicted sensitivity rankings under controlled parameter changes. Third, repeating the workflow for pseudoinverse, constrained QP, redistributed, and adaptive allocators will show how allocation design could change uncertainty margins.

ACKNOWLEDGMENTS

The research was conducted as part of "Enabling unmanned aerial vehicles (drones) to use tools in complex dynamic environments UOCX2104", funded by the New Zealand Ministry of Business, Innovation and Employment.

REFERENCES

[1] T. P. Nascimento and M. Saska. Position and attitude control of multi-rotor aerial vehicles: A survey. *Annual Reviews in Control*, 48:129–146, 2019.

[2] P. H. M. Souza and K. Stol. Constrained dynamics of an aerial manipulator interacting with flexible cantilever beams. *IEEE/ASME Transactions on Mechatronics*, 28(2):967–975, 2023.

[3] R. Rashad, J. Goerres, R. Aarts, J. B. C. Engelen, and S. Stramigioli. Fully actuated multirotor UAVs: A literature review. *IEEE Robotics & Automation Magazine*, 27(3):97–107, 2020.

[4] Z. J. Chen, J. X. J. Bannwarth, K. A. Stol, and P. J. Richards. Analysis of a Multirotor UAV with Tilted-Rotors for the Purposes of Disturbance Rejection. In *2018 International Conference on Unmanned Aircraft Systems (ICUAS)*, pages 864–873, Dallas, TX, June 2018. IEEE.

[5] M. Bodson. Evaluation of optimization methods for control allocation. *Journal of Guidance, Control, and Dynamics*, 25(4):703–711, 2002.

[6] M. W. Oppenheimer, D. B. Doman, and M. A. Bolender. Control allocation for over-actuated systems. In *2006 14th Mediterranean Conference on Control and Automation*, pages 1–6, 2006.

[7] J. M. Buffington and D. F. Enns. Lyapunov stability analysis of daisy chain control allocation. *Journal of Guidance, Control, and Dynamics*, 19(6):1226–1230, 1996.

[8] J.D. Boskovic and R.K. Mehra. Control allocation in overactuated aircraft under position and rate limiting. In *Proceedings of the 2002 American Control Conference*, volume 1, pages 791–796, 2002.

[9] W. C. Durham. Attainable moments for the constrained control allocation problem. *Journal of Guidance, Control, and Dynamics*, 17(6):1371–1373, 1994.

[10] M.F. Santos, L.M. Honório, A.P.G.M. Moreira, P.A.N. Garcia, M.F. Silva, and V.F. Vidal. Analysis of a fast control allocation approach for nonlinear over-actuated systems. *ISA Transactions*, 126:545–561, 2022.

[11] S. S. Tohidi, Y. Yildiz, and I. Kolmanovsky. Adaptive control allocation for over-actuated systems with actuator saturation. *IFAC-PapersOnLine*, 50(1):5492–5497, 2017.

[12] J. B. Davidson, F. J. Lallman, and W. T. Bundick. Real-time adaptive control allocation applied to a high performance aircraft. In *Society for Industrial and Applied Mathematics*, United States, 2001.

[13] E. J. J. Smeur, Q. P. Chu, and G. C. H. E. De Croon. Adaptive incremental nonlinear dynamic inversion for attitude control of micro air vehicles. *Journal of Guidance, Control, and Dynamics*, 39(3):450–461, 2016.

[14] P. H. M. Souza and K. Stol. Analysis and design of a novel fully-actuated compact multirotor. In *Australasian Conference on Robotics and Automation (ACRA)*, 2021.

[15] A. I. Abouseda, R. O. Doruk, and A. Amini. Parameter identification and speed control of a small-scale BLDC motor: Experimental validation and real-time PI control with low-pass filtering. *Machines*, 13(8):656, 2025.

[16] D. K. Athanasopoulos, P. D. Karagkounis, J. C. Kappatou, and S. Tsotoulidis. Demagnetization faults analysis in a BLDC motor for diagnostic purposes. In *2014 International Conference on Electrical Machines (ICEM)*, pages 1862–1868, 2014.

[17] A. Gong, R. MacNeill, and D. Verstraete. Experimental testing of electronic speed controllers for UAVs. In *2017 IEEE International Conference on Unmanned Systems (ICUS)*, pages 88–93, 2017.

[18] M. Etewa, A. F. Hassan, E. Safwat, M. A. H. Abozied, M. M. El-Khatib, and A. Ramirez-Serrano. Performance estimation of fixed-wing UAV propulsion systems. *Drones*, 8(9):424, 2024.

[19] R. Sanz, P. Garcia, Q.-C. Zhong, and P. Albertos. Robust control of quadrotors based on an uncertainty and disturbance estimator. *Journal of Dynamic Systems, Measurement, and Control*, 138(7):071006, 2016.

[20] T. Bresciani. Modelling, identification and control of a quadrotor helicopter. *Master's Thesis, Lund University*, 2008.

[21] X. Yu, Y. Zhang, and J. Jiang. Experimental study on adaptive control for quadrotors with unknown payload and center of mass offset. *Control Engineering Practice*, 136:105555, 2023.

[22] T. A. Shifat and H. Jang-Wook. Remaining useful life estimation of BLDC motor considering voltage degradation and attention-based neural network. *IEEE Access*, 8:168414–168428, 2020.

[23] J. D. Anderson. *Introduction to Flight*. McGraw-Hill Education, 8th edition, 2016.

[24] N. R. Draper and H. Smith. *Applied Regression Analysis*. Wiley, 3rd edition, 1998.